Pure Appl. Chem., Vol. 77, No. 2, pp. 345–358, 2005.
DOI: 10.1351/pac200577020345

Plasma diagnostics by laser spectroscopic electric field measurement*

U. Czarnetzki[1,‡], D. Luggenhölscher[1], V. A. Kadetov[1], and H. F. Döbele[2]

[1]Institute for Plasma and Atomic Physics, Ruhr-University Bochum, 44780 Bochum, Germany; [2]Institute for Experimental Physics, University Duisburg-Essen, 45117 Essen, Germany

Abstract: Laser spectroscopic electric field measurements have the potential to become a versatile tool for the diagnostics of low-temperature plasmas. From the spatially and temporally resolved field distribution in the sheath close to electrodes or surfaces in general, a broad range of important plasma parameters can be inferred directly: electron temperature; ion density distribution; displacement-, ion-, electron-diffusion current density; and the sheath potential. Indirectly, the electron and ion energy distribution functions and information on the ion dynamics in the sheath can also be obtained. Finally, measurements in the quasi-neutral bulk can also reveal even the plasma density distribution with high spatial and temporal resolution. The basic concepts for analysis of the field data are introduced and demonstrated by examples in hydrogen discharges.

Keywords: plasma diagnostics; plasma sheaths; RF discharges; microwave discharges; laser spectroscopy; electrical field measurement.

INTRODUCTION

In gas discharges or plasmas in general, electric fields play a fundamental role. Power is coupled to electrons, waves are driven, and diffusion of electrons and ions is related to electric fields. Within the sheath in front of surfaces, ions and secondary electrons are accelerated to high energies. Last but not least, the random distribution of charges is the origin of stochastically distributed microfields. Further, electric fields in discharges are directly related to a number of important parameters such as voltages, currents, electron and ion densities, and energy distributions. In particular, the chemistry in many discharges is affected strongly by the ion fluxes and energy distribution in the boundary sheath and at the surface of walls and electrodes, which are in turn determined by the sheath electric field. Although it is obvious that measurements of electric fields in plasmas can provide a direct insight into the physics of discharges, it turns out to be experimentally rather demanding. Electrical diagnostic techniques are available for the induced electric field in inductively coupled plasmas by so-called B-dot-probes [1], and the ambipolar field can be deduced from Langmuir [2] or emissive probe [3] measurements. In recent years, a number of emission and laser spectroscopic techniques have been developed that allow the nonintrusive measurement of fields in plasmas [4–22]. However, there are only few examples where these techniques have been applied not only for demonstration, but as a real plasma diagnostic technique [4,6,14,15]. Therefore, the intention of this paper is not so much the introduction of a particular spectroscopic scheme, but to demonstrate the potential of electric field measurements for plasma diagnostics.

*Paper based on a presentation at the 16th International Symposium on Plasma Chemistry (ISPC-16), Taormina, Italy, 22–27 June 2003. Other presentations are published in this issue, pp. 345–495.

‡Corresponding author

This requires not only sensitive spectroscopic techniques, but also certain concepts for further analysis of the measured data.

In low-pressure discharges, these concepts are essentially independent of the particular spectroscopic scheme by which the field is measured. Electric fields in low-pressure discharges might be divided into six categories: (a) fields in the high-voltage sheath free of electrons, (b) fields in the Debye sheath with the electron density comparable to the ion density, (c) drift fields, (d) microfields in the quasi-neutral bulk which scale with the plasma density, (e) microwave fields (or wave fields in general), and (f) ambipolar fields. Examples for the analysis of electric field measurements are presented for all categories except for the ambipolar fields, which are by far too low, usually even substantially lower than the microfields. The spectroscopic technique applied here is fluorescence-dip spectroscopy on Rydberg states of atomic hydrogen [12].

SPECTROSCOPIC SCHEMES

Schemes for laser spectroscopic electric field measurements are almost all based on the Stark effect in Rydberg states of neutral atoms or molecules. In Rydberg states, bounded electrons are relatively remote from the nucleus, and, therefore, even weak external fields can have a strong effect on the electron motion. Generally, the Stark effect leads to new atomic/molecular wave functions and energies, where the wave functions can usually be represented as a superposition of different angular momentum states with the same principle quantum number.

The mixing of states can allow for observation of "forbidden" transitions where the ratio of the line strengths of allowed and forbidden transitions is a measure of the field strength. This is the case especially in diatomic molecules like BCl [4], BH [18], CS [11], and NaK [7]. The first laser spectroscopic field measurements were actually performed on BCl in a BCl_3 discharge by Gottscho in the mid-1980s.

The new eigenstates with their field-dependent energies can often be observed directly as a splitting of a particular transition into a number of so-called Stark components. Here, the separation or the shift of the Stark components is the measure for the field strength. The most prominent example is atomic hydrogen, since the Stark effect is calculated relatively easily and, even more important, scales linear with the field even at relatively low field strengths [10,12]. The width of the spectrum of Stark components increases with the principal quantum number n like n (n-1). Therefore, Rydberg states with high n are particularly sensitive. The linear scaling with the field is a consequence of the degeneracy of the energies of angular momentum states with the same principle quantum number. In noble gases (He, Ne, Ar, Kr, Xe) this is not the case, and the Stark effect becomes quadratic at low field strengths, which gives at a similar principal quantum number a lower sensitivity than in atomic hydrogen [5,6,8,9,14,17,19,20]. Further, the spectra are generally more complex. Nevertheless, there has been substantial progress in recent years on both, the development of sensitive experimental techniques and the precise calculation of the splitting. It should be noted, that only Kr and Xe can be excited from the ground state and that a sufficient population of metastable states is required for measurements in He, Ne, and Ar. The field sensitivity depends strongly on the particular scheme and ranges between a few V/cm to a few 100 V/cm.

Alternative techniques not based on the Stark effect are coherent anti-Stokes Raman scattering [21], a four-wave mixing technique, in H_2 at atmospheric or higher pressures and ion drift measurements, which have been performed especially on Ar^+ [22]. The latter technique is based on the determination of the Doppler shift of ion resonance lines. It is the only technique that allows inferring indirectly the strength and direction of the weak ambipolar field.

In this paper, neutral hydrogen atoms in the plasma serve as probes for the local electric field strength. The atoms are excited in a first step by a Doppler-free two-photon excitation at $\lambda = 205$ nm to $n = 3$ and fluorescence light at Balmer-α ($\lambda = 656$ nm) is observed (Fig. 1). In a second step, the atoms

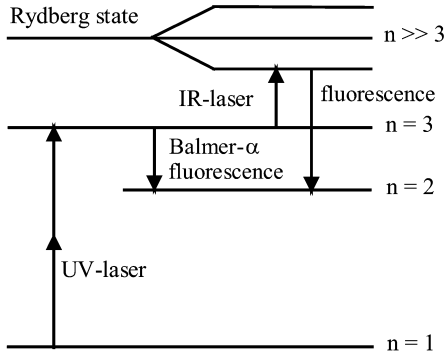

Fig. 1 Scheme for electric field measurement in atomic hydrogen by the fluorescence-dip technique.

are further excited by a tunable infrared beam around λ = 850 nm to the Rydberg state (typically, n = 14–30). When this radiation is in resonance with a transition to a Stark shifted level, population is transferred from n = 3 to the Rydberg state, and the fluorescence at Balmer-α decreases accordingly. Therefore, the spectrum is represented as a series of dips in the fluorescence intensity. The field strength is inferred from a comparison of the measurement with calculated spectra.

With this technique, in principle any Rydberg state is within convenient tuning range for the infrared laser. However, the main advantage of the technique is the fact that it does not depend on the lifetime of the Rydberg state. The lifetime scales with the third power of n, while the Stark splitting scales like n^2. However, states with a long lifetime are very unfavorable for fluorescence measurements since the emission is difficult to discriminate from noise or background radiation. Therefore, fluorescence light originating from Rydberg states with high n, which are very sensitive to the electric fields, cannot be observed practically in a gas discharge. The fluorescence-dip technique is a convenient way to overcome this constraint. The technique allows the sensitive measurement of fields down to 5 V/cm with high spatial (60 μm) and temporal (5 ns) resolution. Further potential candidates for the application of this technique are other atomic radicals such as N, O, and Cl.

EXPERIMENTAL SET-UP

Measurements were performed either in an alternatively capacitively or inductively coupled Gaseous Electronics Conference (GEC) cell at the standard radio frequency (rf) of f = 13.56 MHz or in a commercial slot antenna microwave plasma source (SLAN) microwave reactor at f = 2.45 GHz. Details of the GEC cell, the SLAN reactor, and the laser system can be found in [23], [24], and [14], respectively.

In the case of capacitive coupling (CCP), the upper electrode is grounded and the rf power is applied to the lower electrode. The electrode diameter is 10 cm, and the separation is 2.5 cm. In the case of inductive coupling (ICP), the upper electrode is replaced by a planar bifilar antenna coil of 12-cm diameter inside a monolithic quartz cylinder. The surface of the quartz window is 5 cm above the lower electrode, which is grounded in this case. A combined ion energy and mass analyzer (Balzers PPM 421) is incorporated in the water-cooled aluminum electrode. The unfocused laser beams are aligned parallel to the electrode surface, and the fluorescence light is imaged perpendicularly by either an f = 50 mm lens (CCP) or an f = 80 cm lens (ICP) onto a gated ICCD camera (Princeton Instruments). The spatial resolution in the vertical direction is 100 μm and 60 μm, respectively. The unfocused laser beams allow fields to be measured in parallel within a width of up to about 3 mm. At each spectral position, fluorescence light is accumulated over several 100 laser shots, and typically 100 spectral points are recorded for a full spectrum. The laser is locked to the rf phase, and spatial field profiles are measured in small temporal steps of a few ns over the full period of the rf cycle.

In the case of the SLAN reactor, the microwave power at 2.45 GHz is distributed around a waveguide ring resonator. At the inner side of this ring, the microwave is coupled to the plasma by 10 slit antennas. These antennas are separated by half a wavelength. The plasma is confined in a quartz cylinder of 16-cm diameter. The laser beam is sent through the antenna slits across the discharge, and fluorescence light is observed by an ICCD camera from above. Data acquisition is similar to the case described above.

HIGH-VOLTAGE RF SHEATHS

In sheaths with a potential substantially higher than the kinetic energy of the electrons, the electron density is negligible compared to the ion density, electric fields are rather strong (typically higher than a few 100 V/cm), and the sheath width is typically of the order of a few mm up to one cm in low-pressure discharges. This simplifies very much the measurement and further analysis of the electric field profiles. However, the situation is more complex when the voltage is time-dependent, as is the case especially in rf discharges. The high temporal resolution of the laser spectroscopic technique on an ns scale allows temporally resolved measurements of the sheath dynamics in rf discharges at the standard frequency of $f = 13.56$ MHz, corresponding to a period of $T = 74$ ns. Further, the detection of the fluorescence light by an ICCD camera provides synchronous recording of the two-dimensional field distribution across the sheath in front of an electrode.

A demonstration of this capability of two-dimensional field mapping is given by a measurement performed on a structured electrode covered with a thin dielectric (Fig. 2). The trenches are 2 mm deep and 5 mm wide, and the bar in between has the same width. The thickness of the BK7 glass plate is 0.6 mm. The depletion of the field strength above the rightmost bar was caused by a small gap between the bar and the dielectric, leading to a micro discharge between the electrode and the dielectric. This was confirmed by an inspection performed after the experiment that showed a clear deposition pattern at this point on the backside of the glass plate. The discharge is operated in pure hydrogen at a pressure of $p = 50$ Pa and at a capacitive rf power of $P = 80$ W. The peak-to-peak voltage is $U_{pp} = 960$ V and the bias voltage $U_B = 390$ V. The laser pulses are synchronized with the rf phase, and the measurement is performed at the time of maximum negative voltage applied at the electrodes. As expected, the field distribution is strongly influenced by the underlying surface structure. The spatial modulation penetrates, under our discharge conditions, up to 4 mm into the sheath. Of course, above plane electrodes, conditions are by far more homogeneous, although we could observe strong edge effects.

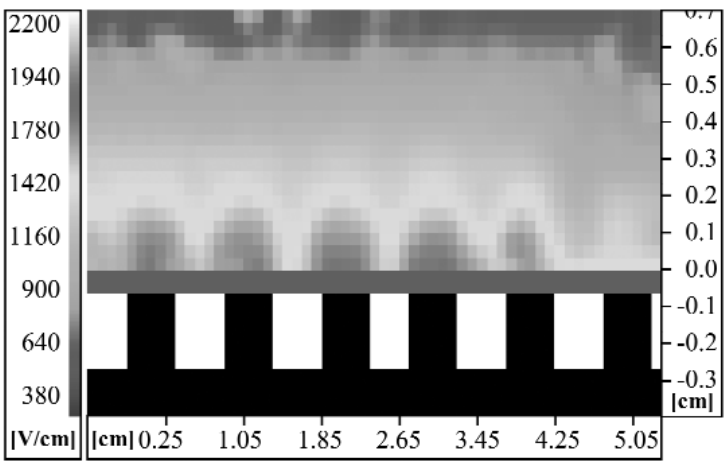

Fig. 2 Absolute value of the electric field in front of the structured aluminum electrode. The electrode is sketched at the bottom of the figures.

An example of the temporal evolution of the axial field distribution in the center above a planar electrode at p = 80 Pa and P = 50 W is shown in Fig. 3. The net-charge density shown on the right is calculated from the measured field by Poisson's equation. The dynamics is presented exemplarily by four selected times within the first half of the rf period. The sheath constriction and the development of a field reversal, i.e., a field attracting electrons toward the electrode, are clearly visible. This field reversal is closely related to a small amount of negative excess charge accumulating at a point close to the sheath edge while quasi-neutrality is reached everywhere else. At early times, the better part of the sheath region (excluding only the sheath edge) is effectively electron-free, and the net-charge density is identical to the ion density. The flat spatial profile is surprising on a first glance, but can be explained by additional ionization within the sheath and especially close to the electrode during the field reversal period. A more detailed discussion of this process can be found in ref. [14].

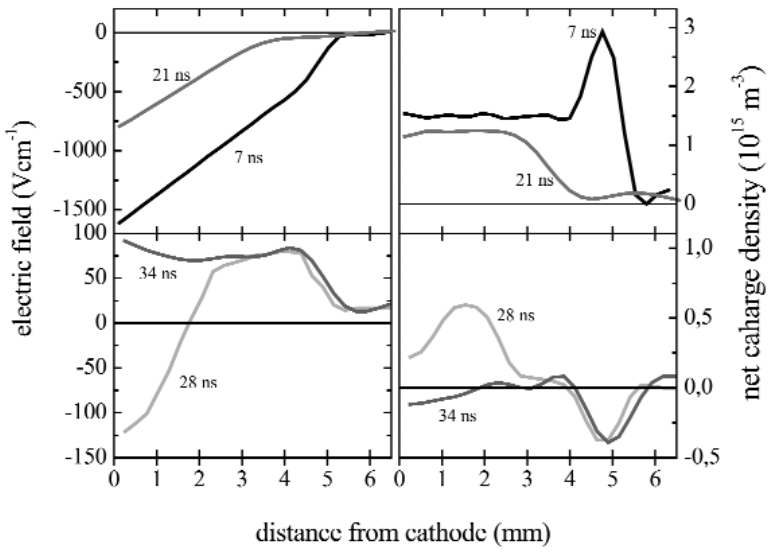

Fig. 3 Spatial distribution of the field and the net-charge density over the first half of the rf period at the powered electrode. The time t = 0 corresponds to a maximum negative potential.

The sheath voltage is inferred by integrating the field across the sheath. Since the voltage drop across the plasma is small, the sum of the voltages measured over the sheaths at the powered and the grounded electrode can be compared with the applied voltages. This is shown in Fig. 4. The slight deviation between the laser measurement and the electrically measured voltage around t = 40 ns is actually an artefact. The electrically measured voltage is reduced slightly at the time of maximum current change by the final inductance of the electrode connections in the GEC reactor.

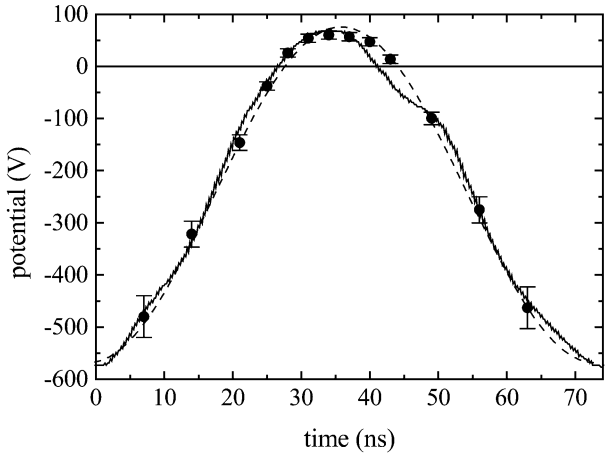

Fig. 4 Voltage applied to the capacitively coupled rf discharge: inferred from the field measurements (dots and solid line), electrical measurement (broken line).

The displacement current density is inferred directly by the temporal derivative of the electric field. This analysis is applied in particular to the fields close to the surface of the electrode. The result for the powered electrode is shown in Fig. 5. After about half the rf period, a sudden reduction of the current amplitude followed by a reversal of the sign is observed. This is the period of the field reversal where a real electron current is flowing to the electrode.

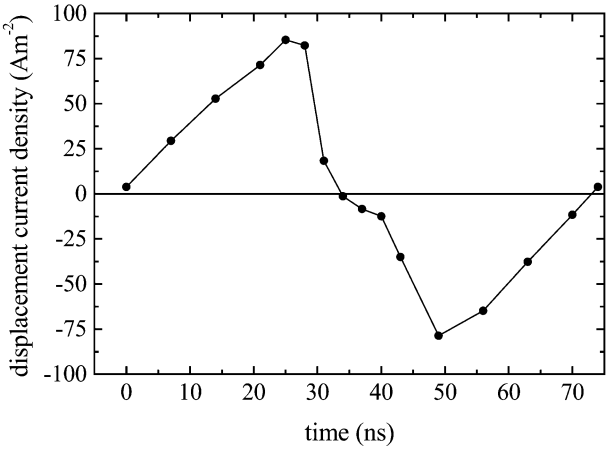

Fig. 5 Displacement current density.

DEBYE SHEATHS

Close to the sheath edge or in sheaths with very low potentials (e.g., floating potential) the electron density is of the same order as the ion density and decreases only gradually from the sheath edge toward the electrode. These regions are characterized further by low fields, typically 100 V/cm and less, and a small spatial extension of about 10 times the Debye length λ_D, typically about 1 mm. In low-pressure discharges, Debye sheaths can usually be considered as collisionless for ions. Investigations of these regions require a good field sensitivity, high spatial resolution, and in the case of dynamics, also a good temporal resolution. Further, for further analysis of the field data, the special features of the Debye

sheath require an approach, which is different from the case of high-voltage sheaths. Here, we present first measurements in the Debye sheath and some novel analysis techniques.

The measurements were performed in an inductively coupled rf discharge at 13.56 MHz at the sheath above the grounded electrode. Field measurements are performed in pure hydrogen at a pressure of p = 10 Pa and an rf power of P = 300 W. Under these conditions, the discharge is in the inductive mode with a small but final residual CCP. At a pressure of p = 10 Pa the dominant ion is H_3^+ with a large mean-free path of about λ = 1 cm at typical ion energies at the sheath edge of E_i = 1 eV. Therefore, within the sheath, ions are collisionless and, due to inertia, respond essentially only to the DC (time averaged) component of the sheath potential.

Spatial profiles of the measured electric field distributions for different phases of the rf are shown in Fig. 6. The sheath width is only s = 1 mm, and the fields are relatively low with a moderate temporal modulation. In particular, the field never vanishes completely and can be described by a DC component with some small residual rf component. The spectra are blurred close to the electrode surface, and, therefore, this region is excluded from the data analysis.

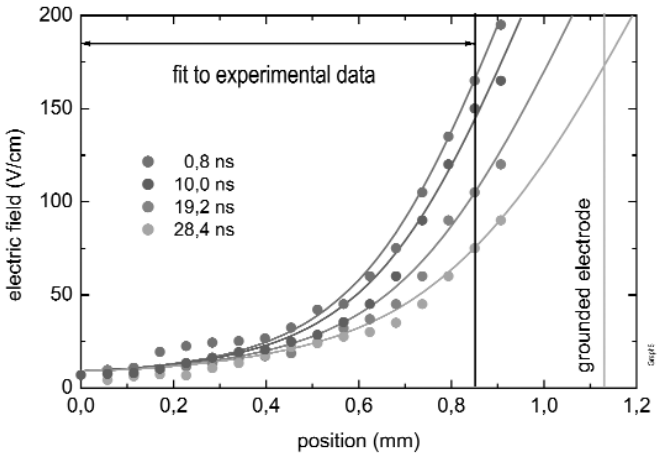

Fig. 6 Measured electric field distribution in the sheath for various times during the constriction phase. The solid lines are fits by a numerical calculation.

The electron temperature and the plasma density at the sheath edge can be deduced from the measured fields by the Poisson equation, if a Boltzmann distribution $n_e(T_e)$ is assumed for the low-energy electrons ($E_e < 2\ kT_e$), which contribute to the sheath electric field. The ion density $n_i(T_e)$ is related directly to the electron temperature and the potential in the sheath by particle and energy conservation. n_i as well as n_e are proportional to the plasma density at the sheath edge n_0 where $n_e = n_i = n_0$. Now a quantity $\sigma^2(T_e, n_0)$ can be defined by the difference of the squares of the left and the right side of the Poisson equation:

$$\sigma^2\left(T_e, n_0\right) = \sum_{x,t=1}^{X,T} \left\{ n_0 \left[\left(\frac{n_i\left(T_e\right)}{n_0} \right)_x - \left(\frac{n_e\left(T_e\right)}{n_0} \right)_{x,t} \right] - \frac{\varepsilon_0}{e} \left(\frac{\partial E}{\partial x} \right)_{x,t} \right\}^2 \tag{1}$$

The sum is taken over all spatial points and all times (rf phases). The value of $\sigma^2(T_e, n_0)$ depends strongly on the choice made for the two parameters T_e and n_e, which can be varied numerically. The minimum yields the real values of electron temperature and density. The result of this procedure is shown in Fig. 7. In our case, the electron temperature is also known from the ion energy spectrum of H^+ to be T_e = 2.2 eV. The agreement within 10 % is remarkable, although the uncertainty of the elec-

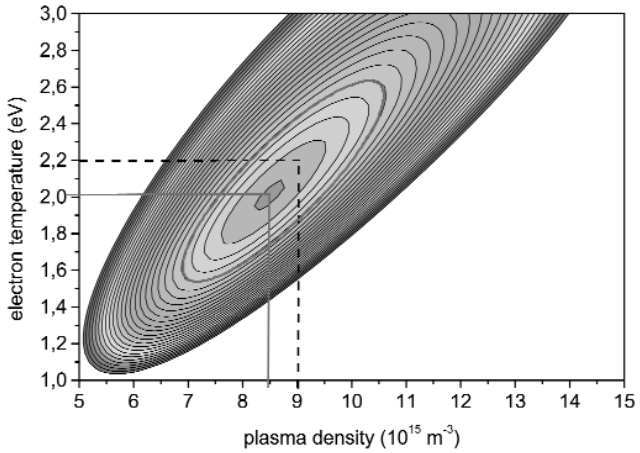

Fig. 7 Electron temperature and density inferred from the field measurement by the minimum of σ^2. The independently obtained temperature of T_e = 2.2 eV (Langmuir probe) results in a slightly higher density.

tron temperature is larger than for the density. The result is: $n_0 = 9.1\ 10^{15}$ m^3 at $T_e = 2.2$ eV. The time-independent ion current density follows from the Bohm criterion as $j_i = 12$ A/m^2.

By applying current and energy conservation, one can then infer directly the relative ion density within the sheath from the measured data and the known electron temperature. Since on the average (over one rf period) there is no net current flowing to the electrode, further, the dynamic floating potential condition applies. This yields the relative ion density at the electrode surface, which depends mainly on the ion mass and only weakly on the ratio of the dynamic potential and the electron temperature. For comparison, Fig. 8 shows also the result inferred from the Poisson equation, when the above values for T_e and n_0 are inserted.

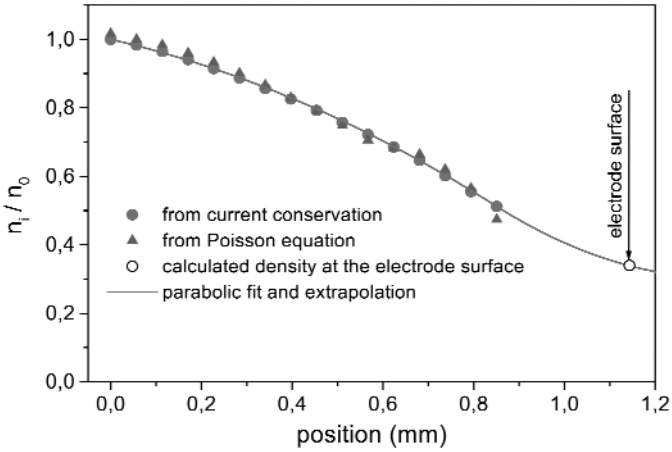

Fig. 8 Relative ion density in the sheath obtained directly from the measured field (dots) and by the Poisson equation for T_e = 2.2 eV and $n_0 = 9.1\ 10^{15}$ cm^{-3} (triangles). The electrode position is indicated. The density is interpolated by a parabola in the region between the last measured point and the surface.

The assumption of a Boltzmann distribution can be justified a posteriori self-consistently by calculation of the relative electron density as a function of the potential for various phases from the Poisson equation on the basis of the measured data and the inferred values for T_e and n_0. For each phase, the position within the sheath is converted to the potential. The result is shown in Fig. 9, where it is com-

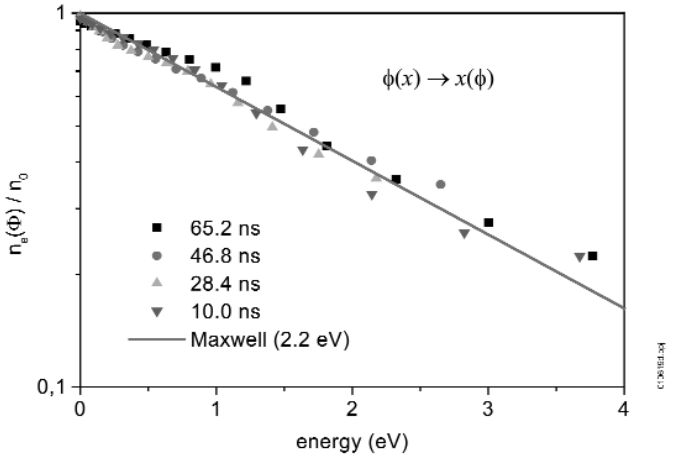

Fig. 9 Relative electron density as a function of the sheath potential as obtained from the field measurement for different rf phases, solid line: Boltzmann distribution for T_e = 2.2 eV.

pared to a Boltzmann distribution with T_e = 2.2 eV. Clearly, the distribution is well described by the Boltzmann factor for electron energies up to 4 eV. The result agrees also well with a Langmuir probe measurement performed at the edge of the electrode where a slightly higher temperature (T_e = 2.4 eV) and a density of $n_e = 4.3\ 10^{11}$ cm^{-3} is obtained. An extrapolation of the density obtained at the sheath edge toward the probe position by a simple collisional pre-sheath model yields the same density and confirms the accuracy of the measurement and the analysis.

Essentially, the same procedure might also be applied to the edge of high-voltage sheaths. Even in cases where the sheath itself is collision dominated, the much smaller region of the Debye sheath might still be considered as collisionless. Further, the much stronger temporal variations at the edge of high-voltage rf sheaths should also not alter the validity of the general procedure substantially.

On the basis of the spatial ion density distribution, one can now extrapolate the electric field beyond the last measured point up to the electrode surface. The Poisson equation is integrated numerically with time-dependent boundary conditions: At a given phase, the electric field at the sheath edge is chosen so that an optimum fit (least mean square) to the measured data is obtained. The resulting field distributions are displayed in Fig. 6 as solid lines. From the spatially integrated fields, the time-varying sheath potential results directly (Fig. 10). Clearly, the potential variation is sinusoidal and the accuracy is of the order of a few 100 mV.

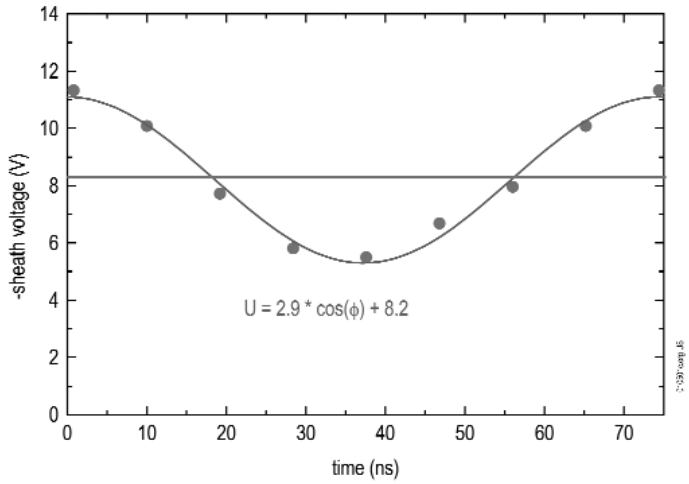

Fig. 10 Sheath voltage.

Finally, the ion energy distribution can be inferred from the calculation of the ion trajectories within the sheath for different start phases on the basis of the known potential. The ions start at the sheath edge with the Bohm velocity for all phases. The result for H_3^+ ions, the dominant species, is displayed in Fig. 11. The result compares well with measurements by an ion energy analyzer (Balzers plasma monitor).

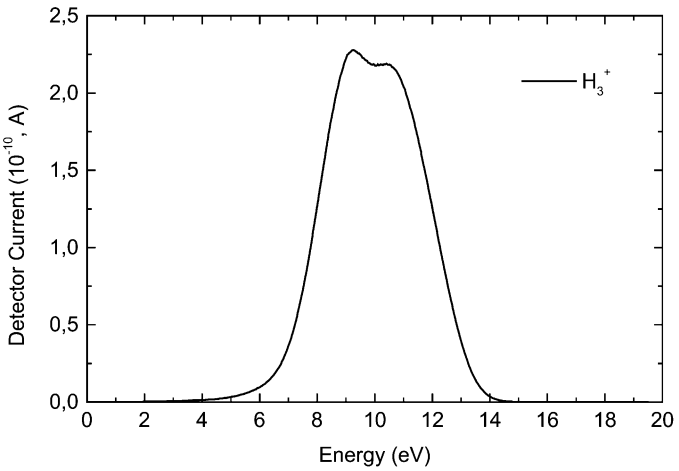

Fig. 11 Ion energy distribution functions for H_3^+ ions obtained from the field measurement.

DRIFT FIELDS

At low pressures of some 10 Pa or below, fields driving an electron drift current through the plasma bulk are usually well below 10 V/cm and, therefore, are not accessible to present-day laser spectroscopic techniques. In addition, the plasma microfield is usually of the same order or stronger, so that even with a more sensitive technique, it would be difficult to separate the directed drift field from this isotropic background. However, as demonstrated above, the capacitively coupled rf discharge in hydrogen shows a short period of field reversal (about 15 ns) where a strong drift current is flowing. The fields within the sheath are of the order of several 10 V/cm, and the corresponding potential is of the order of sev-

eral 10 V. The current density can be inferred from the field amplitude, the electron density in the sheath ($1.5\ 10^{15}$ m^{-3}), and the electron mobility ($50\ V^{-1}m^2s^{-1}$) taken from the literature [25]. Here, the electron density is identical to the ion density due to quasi-neutrality in the sheath (see Fig. 3). It is assumed that owing to ion inertia, the ion density is basically time-independent and identical to the value obtained at times of a high sheath potential when the electrons are removed and the density can be deduced by Poisson's equation. The electron current density is shown in Fig. 12. Alternatively, the electron current at the powered electrode can be derived from the difference between displacement current at the powered and the grounded electrode. The result agrees very well with the previous analysis. The peak drift current density is about $j = 100$ A m^{-2}.

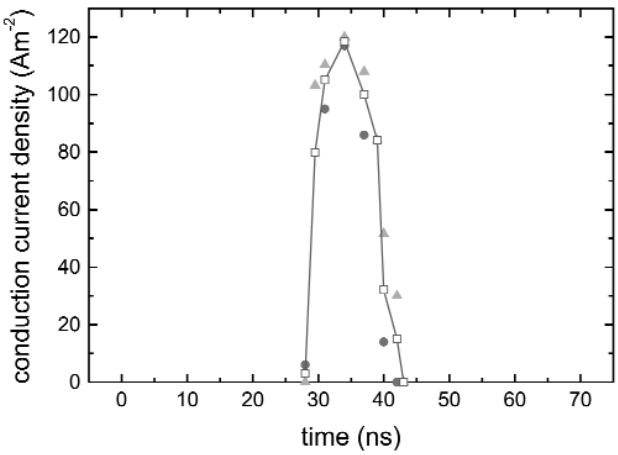

Fig. 12 Drift field during the field reversal phase in the capacitively coupled rf discharge in hydrogen.

MICROFIELDS

In the quasi-neutral bulk of the plasma and in the absence of currents, no directed fields exist (neglecting weak ambipolar diffusion fields). However, electric fields related to stochastic fluctuations in the local charge density on a scale smaller than the Debye length can also cause a broadening of spectral lines [26]. Cold ions show a static (low-frequency) distribution of local field strengths. For most cases, in low-temperature plasmas this is well approximated by the so-called Holtsmark distribution. The average field of this distribution scales like $\langle E \rangle_H \propto N^{2/3}$, where N is the plasma density. For typical densities in the range between 10^{10}–10^{12} cm^{-3}, the field ranges between 10–100 V/cm and is, therefore, well within the sensitivity of the fluorescence-dip technique in atomic hydrogen. In addition to the quasi-static ion field, fast electrons can give rise to high-frequency, dynamic fields (collisional broadening). This contribution depends on the temperature and the density of the electrons and is neglected here. Experimentally, we see no difference between the line-broadening with hot and cold electrons, which motivates our simplified approach.

Measurements were performed in the SLAN microwave plasma reactor [24]. The gas mixture of argon and hydrogen is argon-rich (10:1). The discharge is pulsed at a frequency of 200 Hz, and the average microwave power (forward–reflected) is 200 W (20 % on, 80 % off).

Emission measurements indicate that a symmetrical discharge is generated with strong emission in front of all antenna slots. This is also well reflected in the line-broadening and the related density profiles (Fig. 13). The plasma density deduced on the basis of the Holtsmark distribution reaches about $n = 10^{12}$ cm^{-3}. This corresponds to a skin depth of about 2 cm, so that the microwave cannot penetrate into the volume. When the microwave power is switched off, the emission vanishes within about 2 μs. However, the line-broadening measured in the plasma decays much slower on a time scale of the order of several ms by recombination and diffusion. This broadening is caused clearly by the microfield of

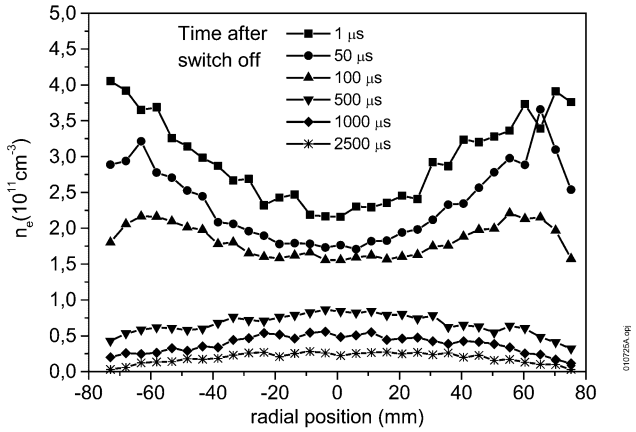

Fig. 13 Decay of the plasma density in the afterglow of the microwave discharge.

the charged particles in the plasma. The profiles in the quasi-stationary on-phase and 10 μs after switch-off are identical. Initially the profiles are concave since the plasma is generated at the edge and the density is reduced in the centre by diffusion along the axis and by recombination. In the late afterglow, the density profile changes to a typical diffusion profile with a maximum in the centre. At these times, the higher diffusion modes have decayed and recombination is negligible at low plasma densities.

MICROWAVE FIELDS

In the very early phase of a microwave pulse (i.e., prior to ignition), the plasma density and the corresponding microfields are still low. Therefore, the skin depth is large and the microwave can fill the entire discharge region. Then, the dominant field is the microwave field until the discharge ignites and the plasma density increases substantially. Only in this early phase, the microwave field can be measured. The fast oscillation of the field is not resolved. Nevertheless, the Stark effect responds only to the absolute value of the field so that the time-averaged value of the field amplitude can be measured. The resulting radial microwave field distribution is shown in Fig. 14.

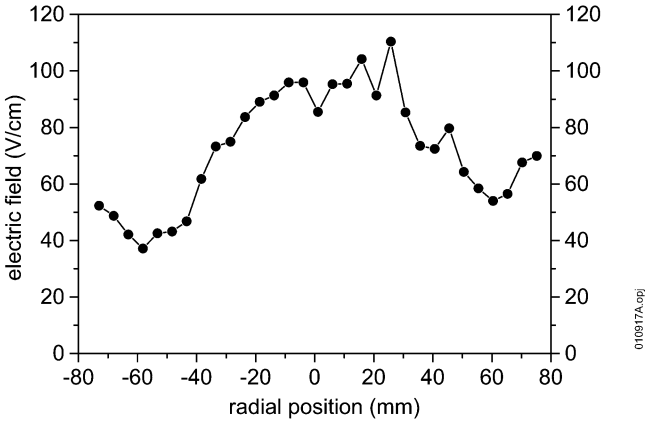

Fig. 14 Radial distribution of the microwave field amplitude prior to the ignition of the discharge.

SUMMARY

It has been demonstrated that laser spectroscopic electric field measurements can offer direct access to a wide range of important plasma parameters. Simple models allow even a further extension to quantities related to the field indirectly, like the ion energy distribution function. Good field sensitivity and high temporal and spatial resolution are required for the laser spectroscopic technique. Depending on the processing gas mixture and the general experimental conditions, alternative schemes in various atomic or molecular systems can be applied. However, the basic concepts for the analysis of the measured field distributions should be rather independent of the particular spectroscopic technique. A demonstration of the potential for plasma diagnostics was given in hydrogen discharges. Although further development is necessary and possible, laser spectroscopic electric field measurements have reached a level where they can establish themselves as a novel versatile tool for plasma diagnostics.

ACKNOWLEDGMENTS

The measurements on the structured electrode were performed together with Dr. G. Hebner from SANDIA in connection with a collaboration supported by the Deutsche Forschungsgemeinschaft in the frame of the Sonderforschungsbereich 191. All other investigations were supported by grants from the Bundesministerium für Bildung und Forschung and by the Ministerium für Schule, Wissenschaft und Forschung des Landes Nordrhein-Westfalen.

REFERENCES

1. R. Piejak, V. Godyak, B. Alexandrovich. *Rev. Sci. Instrum*. **72**, 4002 (2001).
2. F. F. Chen. In *Gaseous Electronics*, Vol. 1, M. N. Hirsch and H. J. Oskam (Eds.), Academic Press, New York (1978).
3. T. Lho, N. Hershkowitz, G. H. Kim. *Rev. Sci. Instrum*. **71**, 403 (2000).
4. R. A. Gottscho. *Phys. Rev. A* **36**, 2233 (1987).
5. B. N. Ganguly. *J. Appl. Phys.* **60**, 571 (1986).
6. E. A. Den Hartog, D. A. Doughty, J. E. Lawler. *Phys. Rev. A* **38**, 2471 (1988).
7. M. P. Alberta, H. Debontride, J. Derouard, N. Sadeghi. *J. Phys. III (France)* **3**, 105 (1993).
8. J. E. Lawler and D. A. Doughty. *Adv. Atom. Mol. Opt. Phys*. **34**, 171 (1994).
9. G. A. Hebner, K. Greenberg, M. E. Riley. *J. Appl. Phys*. **76**, 4036 (1994).
10. J. P. Booth, M. Fadlallah, J. Derouard, N. Sadeghi. *Appl. Phys. Lett*. **65**, 819 (1994).
11. S. Maurmann, V. P. Gavrilenko, H. J. Kunze, E. Oks. *J. Phys. D: Appl. Phys*. **29**, 1525 (1996).
12. U. Czarnetzki, D. Luggenhölscher, H. F. Döbele. *Phys. Rev. Lett.* **81** (21), 4592 (1998).
13. J. B. Kim, K. Kawamura, Y. W. Choi, M. D. Bowden, K. Muraoka, V. Helbig. *IEEE Trans. Plasma Sci.* **26**, 1556 (1998).
14. U. Czarnetzki, D. Luggenhölscher, H. F. Döbele. *Plasma Sources Sci. Technol.* **8**, 230 (1999).
15. U. Czarnetzki, D. Luggenhölscher, H. F. Döbele. *Appl. Phys. A* **72**, 509 (2001).
16. U. Czarnetzki, G. A. Hebner, D. Luggenhölscher, H. F. Döbele, M. E. Riley. *IEEE Trans. Plasma Sci.* **27**, 70 (1999).
17. V. P. Gavrilenko, H. J. Kim, T. Ikutake et al. *Phys. Rev. E* **62**, 7201 (2000).
18. E. K. Cherkasova, V. P. Gavrilenko, A. I. Zhuzhunashvili. *Proceedings Laser Aided Plasma Diagnostics X*, Fukuoka, Japan (2001).
19. K. Takizawa, K. Sasaki, K. Kadota. *Jpn. J. Appl. Phys*. **41**, L1285 (2002).
20. T. J. Jiang, M. D. Bowden, B. Visser, G. M. W. Kroesen. *Proceedings Frontiers in Low Temperature Plasma Diagnostics V*, Villaggio Cardigliano, Italy (2003).
21. O. A. Evsin, E. B. Kupryanova, V. A. Ochkin, S. Yu. Savinov, S. N. Tskhai. *Quant. Electr*. **25**, 278 (1995).

22. L. Oksuz, M. A. Khedr, N. Hershkowitz. *Phys. Plasmas* **8**, 1729 (2001).
23. P. J. Hargis, Jr., K. E. Greenberg, P. A. Miller et al. *Rev. Sci. Instrum*. **65**, 140 (1994).
24. F. Werner, D. Korzec, J. Engemann. *Plasma Sources Sci. Technol*. **3**, 473 (1994).
25. A. Gilardini. *Low Energy Electron Collisions in Gases*, John Wiley, New York (1972).
26. H. R. Griem. *Spectral Line Broadening by Plasmas*, Academic Press, New York (1974).